Atmospheric Research 309 (2024) 107574

Contents lists available at ScienceDirect

Atmospheric Research

journal homepage: www.elsevier.com/locate/atmosres

Distinct propagating and standing modes of tropical intraseasonal variability as represented by the two principal oscillation patterns

Jie Wu [a,b], Hong-Li Ren [c,*], Fei-Fei Jin [d], Xiaofeng Xu [a], Li Guo [a]

[a] China Meteorological Administration Key Laboratory for Climate Prediction Studies, National Climate Center, Beijing 100081, China
[b] Collaborative Innovation Centre On Forecast and Evaluation of Meteorological Disasters, Nanjing University of Information Science and Technology, Nanjing 210044, China
[c] State Key Laboratory of Severe Weather, and Institute of Tibetan Plateau Meteorology, Chinese Academy of Meteorological Science, Beijing 100081, China
[d] Department of Atmospheric Sciences, University of Hawaii at Manoa, Honolulu, HI 96822, USA

ARTICLE INFO

Keywords:
Tropical intraseasonal variability
Eastward propagating mode
Standing dipole mode
Principal oscillation pattern
Moisture structure

ABSTRACT

Although the tropical intraseaonal variability (TISV), as the most important predictability sources for subseasonal-to-seasonal (S2S) prediction, is dominated by Madden-Julian oscillation (MJO), its significant fraction does not always share the canonical MJO features, especially when the convective activity arrives at Maritime Continent. In this study, using principal oscillation pattern (POP) analysis on the combined fields of daily equatorial convection and zonal wind, two distinct leading TISV modes with relatively slower *e*-folding decay rates are identified. One is an oscillatory mode with the period of 51 days and *e*-folding time of 19 days, capturing the eastward propagating (EP) feature of the canonical MJO. The other is a non-oscillatory damping mode with *e*-folding time of 13.6 days, capturing a standing dipole (SD) with convection anomalies centered over the Maritime Continent and tropical central Pacific, respectively. Compared to the EP mode, the leading moisture anomalies at low level to the east of convection center are diminish for the SD mode, and instead, the strong negative anomalies of moisture and subsidence motion emerge in the tropical central Pacific area, which may be responsible for the distinct propagation features. Without filtering methods used, timeseries of the two POPs could be applied to the real-time monitoring of EP and SD events in the phase-space diagram. The two modes can serve as the simple and objective approach for a better characterization for diverse natures of TISV beyond the canonical MJO description, which may further shed light on dynamics of the TISV and its predictability.

1. Introduction

Tropical intraseasonal variability (TISV) is generally referred to a board spectrum of phenomena with the variability longer than synoptic timescales (<10 days) and shorter than a season (90 days) in tropics, which has contributed to bridging the gap between weather forecasting and climate prediction (Lau and Waliser, 2012). Some of TISVs are quasi-periodic but others are non-periodic. The most dominant mode of TISV is the Madden-Julian oscillation (MJO) with 30–80-day timescales, which has been intensively investigated since its discovery in early 1970s (Madden and Julian, 1971, 1972; Zhang, 2005, 2013). However, a large fraction of the total variance of TISV over the Indian Ocean (IO) and western Pacific (WP) Ocean exhibit distinct features from the canonical MJO, which deserve thorough understanding for its mechanisms and potential predictability as well (Hirata et al., 2013; Wei et al., 2023).

Typically, MJO is featured by a large-scale spatial structure of zonal wavenumbers 1–3 with significant signals in its atmospheric circulation, deep convection and other variables, propagating eastwards (at approximately 5 m s^{-1}) from the tropical Indian to Pacific oceans (Salby and Hendon, 1994; Zhang, 2005; Waliser et al., 2009). However, the propagation of convection envelopes for individual MJO events differ considerably from event to event (Wang et al., 2019), especially when encountering the Maritime Continent (MC). In observations, some episodes of large-scale MJO convection moved smoothly from IO through WP, while some events rapidly dissipated over MC and thus failed to propagate eastward as far as the canonical MJO events (Kim et al., 2014; Feng et al., 2015; Kerns and Chen, 2016; Zhang and Ling, 2017; Wu et al., 2023). The weakening and blocking of the MJO convection over

* Corresponding author at: State Key Laboratory of Severe Weather, and Institute of Tibetan Plateau Meteorology, Chinese Academy of Meteorological Science, Beijing, 100081, China
E-mail address: renhl@cma.gov.cn (H.-L. Ren).

https://doi.org/10.1016/j.atmosres.2024.107574
Received 28 February 2024; Received in revised form 17 June 2024; Accepted 5 July 2024
Available online 14 July 2024

MC are denoted as the "barrier effect" on the MJO propagation (Inness and Slingo, 2003; Seo and Wang, 2009; Kim et al., 2016). Also, some other events presented absent or very weak convection anomalies over most of IO but significantly intensified convection over MC (Hsu and Lee, 2005; Hirata et al., 2013; Fu et al., 2018; Wang et al., 2019). Focusing on the diverse features of MJO propagation, Feng et al. (2015) divided MJO into eastward-propagating (EP) and non-propagating (NP) types, and Wang et al., 2019 further examined such a diversity by cluster analysis for four archetypes: standing, jumping, slowly eastward propagation and fast eastward propagation types. However, these different types of MJO identified by filtering mothed can only be determined by retrospective analysis (Feng et al., 2015; Zhang and Ling, 2017; Wang et al., 2014; Wei et al., 2023), and some of the diverse features are clearly contradicted to the canonical conceptual paradigms of MJO and may be identified as totally distinct forms of TISV. Therefore, questions are whether there exists intrinsic non-propagating TISV modes, and by which it could be objectively real-time identified?

Wheeler and Hendon (2004; WH04 hereafter) developed a unique real-time multivariate MJO (RMM) indices with outgoing longwave radiation (OLR), 850- and 200-hPa zonal wind anomalies to quantitatively measure MJO activity, without a band-pass filtering used. The RMM indices can capture the fundamental MJO characteristics well and have been widely employed in operations to monitor the real-time MJO evolution (Gottschalck et al., 2010) and evaluate the MJO prediction performance (Lin et al., 2008; Wang et al., 2014; Zhu et al., 2015; Vitart, 2017; Wu et al., 2016; Kim et al., 2018; Jiang et al., 2020; Lim et al., 2018). However, the RMM indices only reflect the first two empirical orthogonal functions (EOFs) with ~25% of the total variance of TISV explained (WH04), discarding the large TISV variance at zonal wavenumbers 2–5 in the higher-order multivariate EOF modes. Liu (2014) ever suggested that the EOFs 3–10 could withhold the power of wavenumbers 2–5 sufficiently, but simultaneously monitoring the first 10 EOFs is complicated and not suitable to operational application. Here, our main motivation is to identify some other distinct TISV modes that occurred previously but with fairly different features from the typical MJO, which will help to understand the diverse characteristics and broad spectrums of TISV beyond the classic MJO conception. Such modes may be non-propagating with large regional impacts but completely missed by the traditional EOF-based analysis and their identification would indicate a new path to improve prospects for the overall TISV predictability.

In this study, we will employ the principal oscillation pattern (POP) analysis to identify the distinct TISV modes with diverse features. Particularly, we intend to show robust evidence for the existence of one long-lasting large-scale convective TISV mode with significantly different features from the canonical MJO, where as an application, the related indices for real-time monitoring can be objectively defined. Investigating such a mode may provide us with better understanding of evolution characteristics and structures of TISV. The remainder of this paper is organized as follows: Section 2 describes data and methodology used. Main results of the POP analysis are shown in Section 3. Details of the evolution and structure characteristics of the POPs are given in Section 4 and one typical case study is presented in Section 5. Summary and discussions are given in Section 6.

2. Data and methodology

2.1. Datasets

Daily-mean datasets of zonal and meridional winds, geopotential height, relative humidity, and vertical velocity are obtained from the National Centers for Environmental Prediction/Department of Energy (NCEP/DOE) Reanalysis II (Kanamitsu et al., 2002). The OLR data are daily-mean value from the National Oceanic and Atmospheric Administration (NOAA) polar-orbiting series of satellites (Liebmann and Smith, 1996). These datasets cover a common time domain from 1 January 1981 through 31 December 2020 in this study.

2.2. Extraction of TISV

We extract the intraseasonal anomalies following the methodology of WH04 and Gottschalck et al. (2010). Firstly, for the three fields, 850-hPa zonal wind (U850), 200-hPa zonal wind (U200) and OLR, their annual cycles are removed by subtracting the individual time mean and the first three harmonics of daily climatology, which are calculated from 1981 to 2010. Then, from the resultant anomaly fields, the interannual components are removed by subtracting previous 120-day mean relative to the target day. Finally, the three intraseasonal anomaly fields are averaged between 15°S and 15°N and normalized using the standard deviations of each field.

2.3. POP analysis

The POP analysis is a multivariate technique to empirically infer characteristics of the space-time variations of a complex dynamical system (von Storch et al., 1988; von Storch and Xu, 1990; von Storch et al., 1995), which has been widely used in diagnosing MJO (Jian, 1995; Newman et al., 2009), El Niño-Southern Oscillation (ENSO; Penland and Sardeshmukh, 1995; Gehne et al., 2014), stratospheric Quasi-Biennial Oscillation (QBO; Xu, 1992) and North Atlantic Oscillation (NAO; Sun et al., 2015). Superior to the EOF analysis that only considers the spatial co-variability of variable fields, the POP analysis can consider the full spatio-temporal structure and here, is applied to investigation of the dominant modes of TISV.

Firstly, the EOF analysis is used to reduce the degree of freedom of the complex system, and then the POP analysis is applied to the principal components (PCs) of the selected leading EOF patterns. The calculation of POPs is mainly following the methodology of von Storch et al. (1995) and Penland and Sardeshmukh (1995). The dynamical system may be described in the form,

$$\mathbf{x}(t+\tau_0) = \mathbf{A}(\tau_0)\mathbf{x}(t) + \mathbf{R} \tag{1}$$

where $\mathbf{x}$ contains the several leading PCs of EOF patterns, τ_0 represents lag days, $\mathbf{A}$ is a linear operator matrix, and $\mathbf{R}$ is a vector of stochastic white noise. The matrix $\mathbf{A}$ can be determined from observed time series $\mathbf{x}(t)$ in terms of an error variance minimization procedure as follows,

$$\mathbf{A}(\tau_0) = \mathbf{C}(\tau_0)\mathbf{C}(0)^{-1} \tag{2}$$

where $\mathbf{C}(\tau_0)$ and $\mathbf{C}(0)$ are the covariance matrices at lag τ_0 and lag 0, defined by.

$$\mathbf{C}(\tau_0) = \langle \mathbf{x}(t+\tau_0)\mathbf{x}^{\mathrm{T}}(t) \rangle \text{ and } \mathbf{C}(0) = \langle \mathbf{x}(t)\mathbf{x}^{\mathrm{T}}(t) \rangle \tag{3}$$

Here, the angle brackets denote an ensemble average, which can be estimated as a time average for variables with stationary statistics.

In general, the matrix $\mathbf{A}$ is not symmetric, some or all of its eigenvalues λ and eigenvectors $\mathbf{p}$ are complex, satisfying $\mathbf{Ap} = \lambda\mathbf{p}$. In most cases, all eigenvalues are different, and the eigenvectors form a linear basis. Therefore, the state $\mathbf{x}$ at any time t can be uniquely expressed in terms of the eigenvectors:

$$\mathbf{x} = \sum_j z_j \cdot \mathbf{p}_j \tag{4}$$

Here, z_j is time coefficient of the eigenvector, which will be conjugate complex if the corresponding eigenvector ($\mathbf{p}_j$) is complex. Then, the contribution $\mathbf{P}(t)$ of the specific complex conjugate pair of ($\mathbf{p}$, $\mathbf{p}^*$) to the process $\mathbf{x}(t)$ can be written as

$$\boldsymbol{P}(t) = z(t)\cdot\boldsymbol{p} + [z(t)\cdot\boldsymbol{p}]^* \tag{5}$$

Insert $\mathbf{p} = \mathbf{p}^r + i\cdot\mathbf{p}^i$, $\mathbf{p}^* = \mathbf{p}^r - i\cdot\mathbf{p}^i$and $z(t) = (z^r(t) - i\cdot z^i(t))/2$ into Eq. (5), $\mathbf{P}(t)$ can be written as

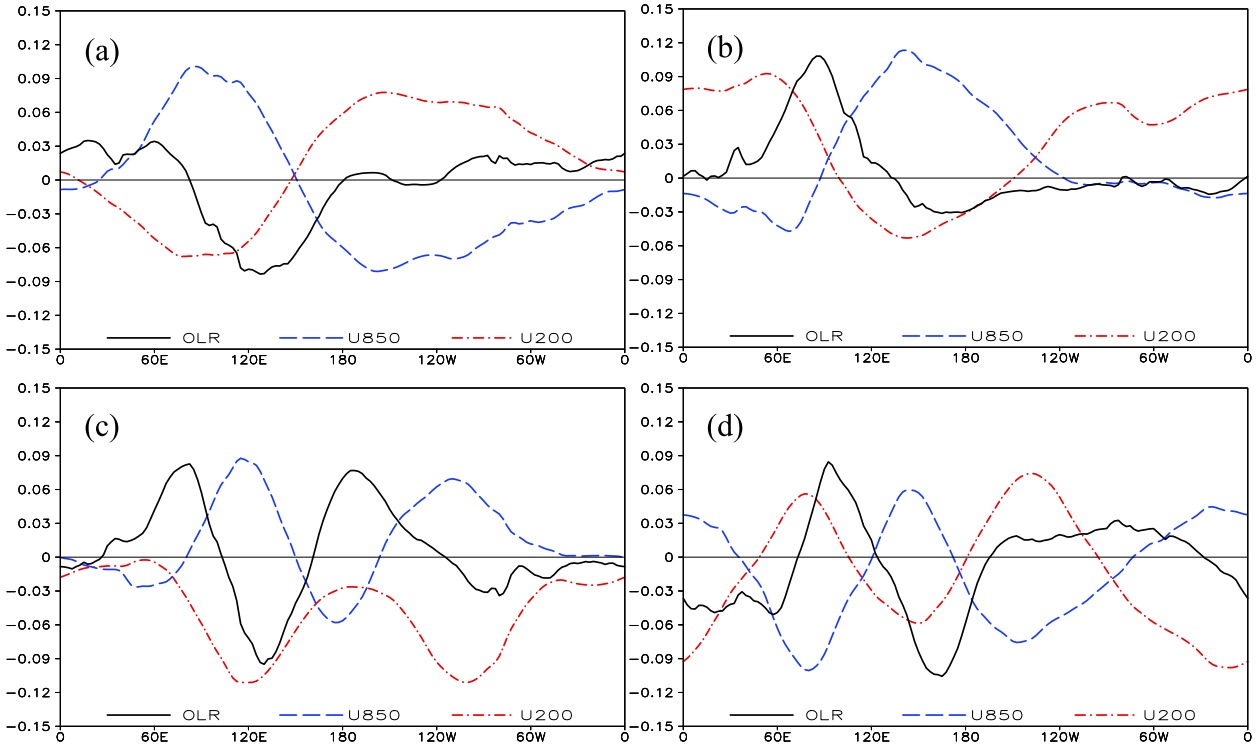

Fig. 1. The spatial structures of the leading 4 EOFs of the combined analysis of OLR, U850 and U200.**a** is EOF1, **b** is EOF2, **c** is EOF3, and **d** is EOF4, respectively.

$$\mathbf{P}(t) = z^r(t)\cdot\mathbf{p}^r + z^i(t)\cdot\mathbf{p}^i = \rho^t\left(cos(\eta t)\cdot\mathbf{p}^r - sin(\eta t)\cdot\mathbf{p}^i\right) \tag{6}$$

with the eigenvalue $\lambda = \rho exp(-i\eta)$ and $z(0) = 1$. Therefore, we can estimate the period and e-folding time of this pair of POP mode as $T = \tau_0 \times 2\pi/\eta$ and $\delta = -\tau_0/ln(\rho)$, respectively. In addition, the POP mode evolves in the consecutive order of

$$\cdots\rightarrow\mathbf{p}^r\rightarrow -\mathbf{p}^i\rightarrow -\mathbf{p}^r\rightarrow\mathbf{p}^i\rightarrow\mathbf{p}^r\rightarrow\cdots \tag{7}$$

If one of the eigenvalues and eigenvectors is real, it means this POP mode will be a non-oscillation damping mode and its contribution to $\mathbf{P}(t)$ can also be written as

$$\mathbf{P}(t) = z(t)\cdot\mathbf{p} = z(0)\lambda^t\mathbf{p} \tag{8}$$

Typically, the time coefficients z is calculated by a least-square fit of the data $\mathbf{x}$ by minimizing

$$\|\mathbf{x} - z\cdot\mathbf{p} - [z\cdot\mathbf{p}]^*\| = \|\mathbf{x} - z^r\cdot\mathbf{p}^r - z^i\cdot\mathbf{p}^i\| \tag{9}$$

However, if more than one POP is identified as long-lasting intrinsic mode, Eq. (9) should be formulated for all the considered POPs ($\mathbf{p}_j$) simultaneously:

$$\|\mathbf{x} - \sum\nolimits_j z_j\mathbf{p}_j\| = min \tag{10}$$

3. Results of the POP analysis

Firstly, we present results of the POP analysis of TISV and derive indices of the leading modes. As mentioned in Section 2, prior to the POP analysis, an EOF analysis is conducted to reduce the degree of freedom of tropical variable fields. Here, the EOF analysis was performed on the meridionally averaged (15°S-15°N) fields of U200, U850 and OLR for the period of 1981–2015. Only the leading 10 EOFs were retained for the POP analysis. Spatial patterns of the first 4 EOFs are shown in Fig. 1. The EOFs 1 and 2 are dominated by the zonal wavenumber 1, while EOFs 3 and 4 are mainly controlled by the zonal wavenumber 2. The higher-order EOF patterns include more complex zonal wave structures (wavenumbers 3–5) (Liu, 2014). The guide of truncating the first 10 EOFs was the fact that they explain >50% variance of raw data (Table 1) and about 87% variance of MJO-filtered data, satisfying our main destination of focusing on the large-scale variability after eliminating small-scale ones. In fact, the following main results are not sensitive to the EOF truncating numbers when we have repeated the calculation with the first 5–20 EOFs truncated.

Then, we perform the POP analysis on the first 10 PCs of EOFs, using Eqs. (2–3) to obtain the matrix $\mathbf{A}(\tau_0)$. In this study, τ_0 was set as 7 days since we mainly focus on intraseasonal time scale, where repeating the

Table 1
Accumulated variance in percentage of the EOF modes.

MODE	Eigenvalues ($\times10^5$)	Accumulated Eigenvalues ($\times10^5$)	Explained Variances (%)	Accumulated Explained variances (%)
1	7.71	7.71	12.23	12.23
2	7.23	14.9	11.47	23.70
3	3.65	18.6	5.78	29.48
4	3.10	21.7	4.92	34.40
5	2.40	24.1	3.80	38.20
6	2.03	26.4	3.22	41.42
7	1.70	27.8	2.70	44.12
8	1.45	29.3	2.30	46.42
9	1.38	30.6	2.19	48.60
10	1.27	31.2	2.02	50.63

Table 2
Properties of principal oscillation patterns.

POP mode	Real-part	Imaginary-part	Decay time (Days)	Period (Days)
1/2	0.69	0.86	18.7	50.8
3	0.60	0	13.6	∞
4	0.32	0	6.11	∞
5/6	0.21	0.70	4.47	63.0
7/8	0.10	0.75	3.10	58.6
9/10	0.15	0.13	3.74	345

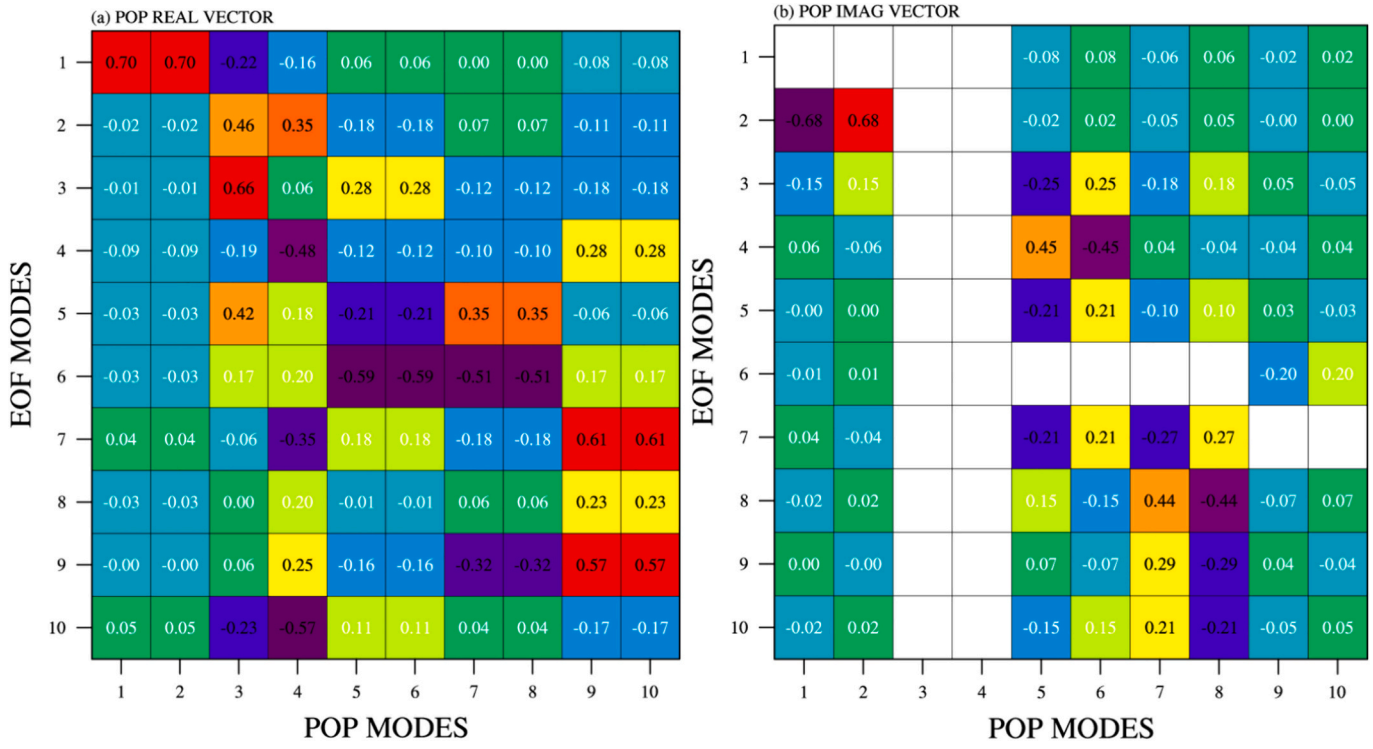

Fig. 2. The **a** real and **b** imaginary eigenvectors of POP modes.

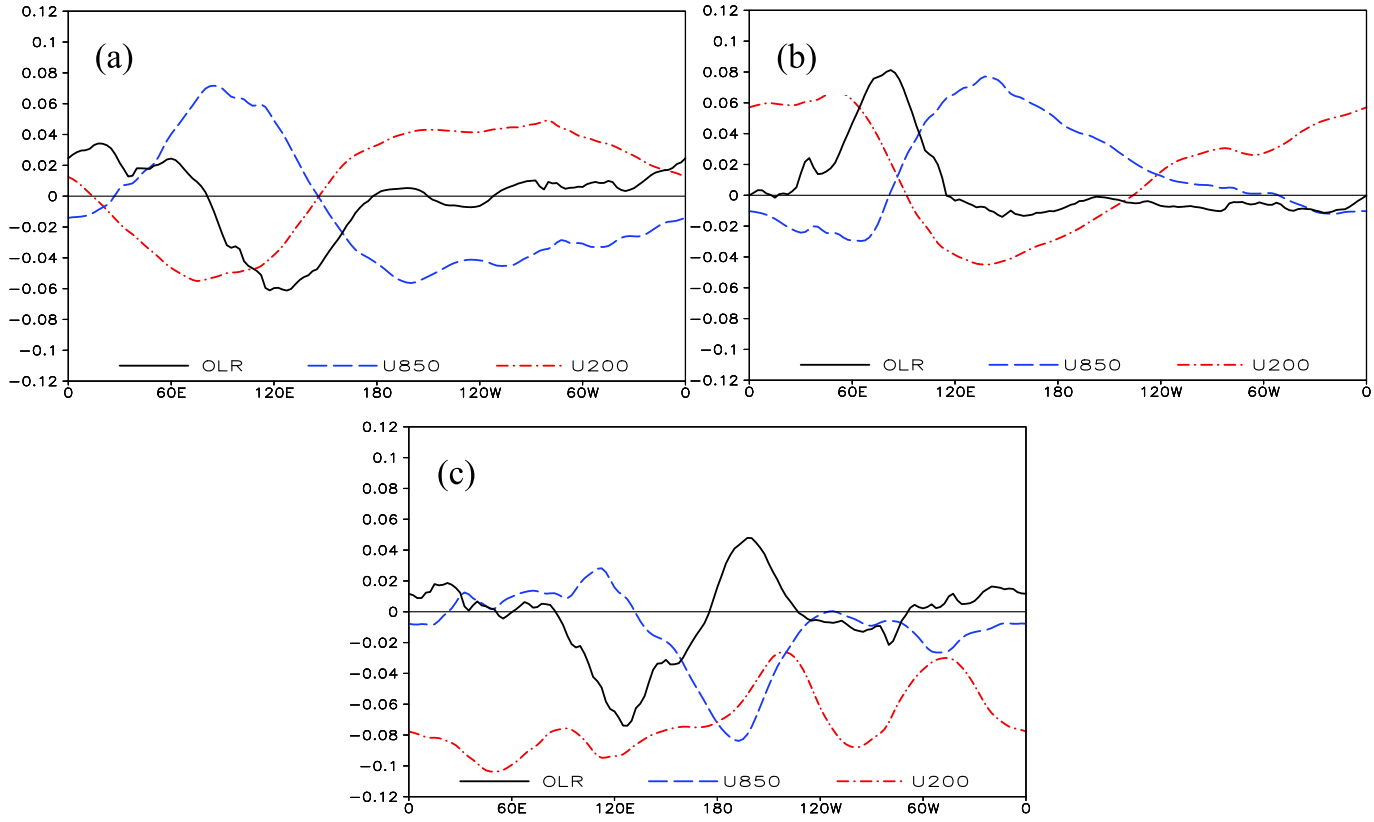

Fig. 3. The leading principal oscillation patterns (POPs) of equatorial OLR, U850 and U200: **a** real-part pattern of POP1 (p_1^r); **b** negative imaginary-part pattern of POP1 ($-p_2^i$), the POPs tend to appear in sequences of the type $p_1^r \rightarrow -p_2^i \rightarrow -p_1^r \rightarrow p_2^i \rightarrow p_1^r$; **c** real-part pattern of POP3 (p_3^r).

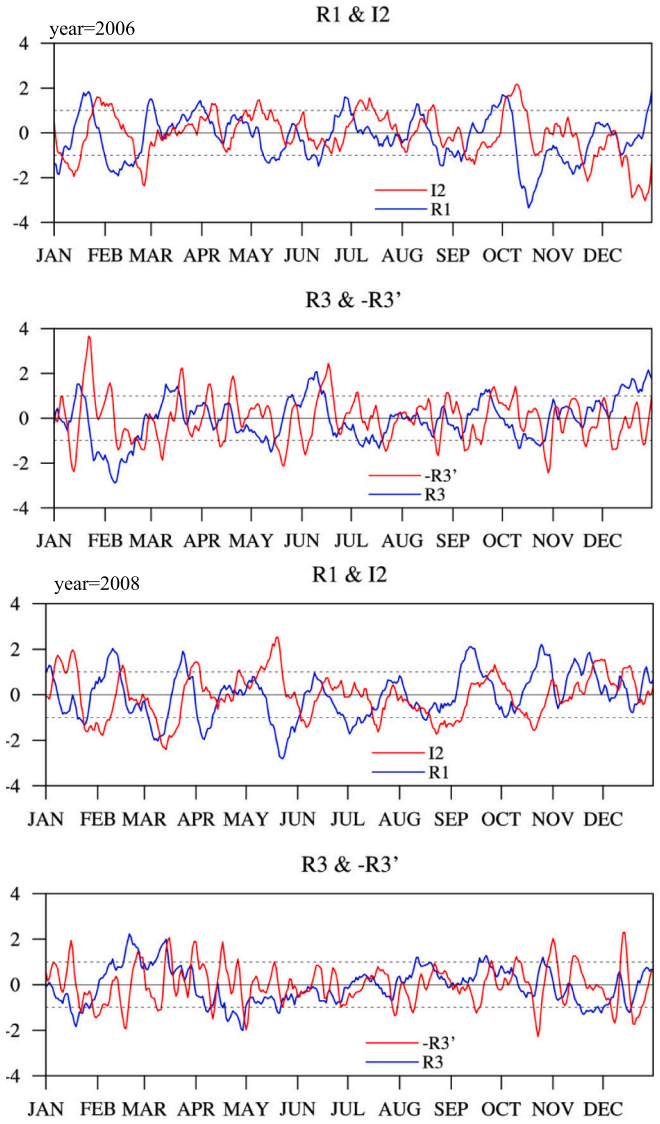

Fig. 4. The time series of normalized POP indices R1, I2, R3, and the time tendency series of R3 (denote as R3') for the year 2006 and 2008. 5-day running mean was applied for R1' and R3'.

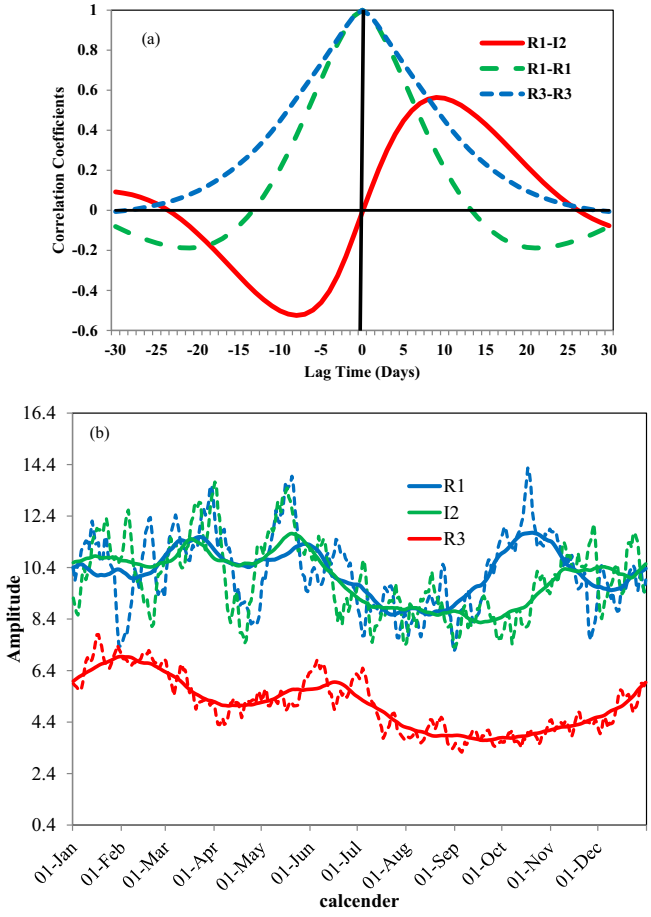

Fig. 5. a Lag correlations between R1 and I2 (solid red line), R1 with itself (dash green line), and R3 with itself (dash blue line). **b** The mean seasonal cycle of standard deviation of POP coefficients R1, I2 and R3 for the 35 years of 1981–2015. 45-day running mean was applied for the solid lines. (For interpretation of the references to color in this figure legend, the reader is referred to the web version of this article.)

analysis at other lag days (τ_0) can still yield similar results. By calculating the eigenvalues λ and eigenvectors **p** of $\mathbf{A}(\tau_0)$, the period and decaying (*e*-folding) time of each POP mode can be estimated following Eq. (6). As shown in Table 2, there are four pairs of oscillatory modes and two purely exponential damping (standing) modes. For the decaying time, the oscillatory mode (POP 1/2) with *e*-folding time of ~19 days and the standing mode (POP 3) with *e*-folding time of ~13.6 days are prominent considering their obviously long-lasting lifetime. These two modes explain 46% and 12.3% total variance, respectively, and their accumulated explained variance is 54.2%, which is not equal to the sum of their individual explained variances due to the facts that the POPs are not exactly orthogonal.

Since we perform the POP analysis on the first 10 PCs, the spatial pattern corresponding to each POP ($\mathbf{P}_g$) can be obtained by

$$\boldsymbol{P}_g^r = \sum_{l=1}^{M} \boldsymbol{P}_l^r \boldsymbol{V}_l, \boldsymbol{P}_g^i = \sum_{l=1}^{M} \boldsymbol{P}_l^i \boldsymbol{V}_l \tag{11}$$

Here, $\mathbf{V}_l$ represents the geographic EOF vectors, $\boldsymbol{P}_l^r$ and $\boldsymbol{P}_l^i$ are the real and imaginary part of eigenvectors (Fig. 2), M is the number of selected leading mode, currently $M = 10$. Following Eq. (11), the convection and circulation geographic patterns of the primary oscillatory and standing POPs are shown in Fig. 3. Mathematically, the POP modes are the linear combination of the first 10 EOFs. Here, we denote the real part and imaginary part patterns of the oscillatory mode (POP1/2) as p_1^r and p_2^i, the real part pattern of the standing mode (POP3) as p_3^r, respectively. The oscillatory mode pattern (Fig. 3a and 3b) is mainly dominated by EOF1 and EOF2 (Fig. 2), which describes the zonal wavenumber 1 with the first baroclinic structure. That is, p_1^r features the enhanced convection locating over MC while $-p_2^i$ shows the enhanced convection locating over the tropical western Pacific, which is about 90° phase shift of p_1^r. The period of this oscillation mode indicates that it will take about 51 days for the evolution of $p_1^r \rightarrow -p_2^i \rightarrow -p_1^r \rightarrow p_2^i \rightarrow p_1^r$. Therefore, this oscillation mode clearly shows the consecutive eastward-propagating feature (denoted as the EP mode), representing the canonical MJO signal in TISV. The difference between EP mode with EOF1 and EOF2 (Fig. 1) is mainly shown by weakening the zonal wind anomalies in the western hemisphere.

The non-oscillatory mode (Fig. 3c) is mainly contributed by EOFs 3, 1, 2, and 4 (Fig. 2), which is featured by a standing dipole pattern of convection anomalies (denote as the SD mode) with the enhanced convection over MC and the suppressed over the tropical central Pacific (CP). Its wind structure is also quite different from that of the EP mode; i.e., in the lower level, the easterly anomalies that control the suppressed convection are much stronger than the westerly anomalies over the active convection area, and in the upper level, the easterly anomalies almost distribute the whole tropical area. Except that, the *e*-folding time

Table 3
Correlation coefficients between POP coefficients and RMM indices.

Indices	RMM1	RMM2	R3
R1	0.964	0.029	−0.211
I2	−0.026	0.903	0.140
R3	−0.062	−0.233	1

of all the other 4 modes is <7 days, much shorter than the above-mentioned EP and SD modes and mainly dominated by larger wavenumbers tropical waves (Figures omitted). These results are highly consistent with that using ERA5 dataset (Table S1, Fig.S1-S2), further confirm the robustness of the dominated POP modes.

Further, Eq. (10) is applied to calculating time series of the POPs. Here, we denote the time coefficients z_1^r, $-z_2^i$, and z_3^r as R1, I2, and R3 for convenience, respectively. Fig. 4 shows the normalized daily R1, I2, and R3 in 2006 and 2008 as an example. As expected from the definition of POPs, I2 shows a clear phase shift with R1 by about 8–15 days lagged, and R3 did not show obvious relation with R1 or I2. Although there still exists some day-to-day noise, the intraseasonal variability is more predominant in all the three timeseries. The lag correlation of R1 and I2 is up to 0.57 when R1 leads at 9 days (Fig. 5a), supporting the oscillatory nature as implied in Eq. (7). The auto-correlation further confirms that $\mathbf{p}_1^r$ and $\mathbf{p}_2^i$ constitute an oscillatory mode with a maximum negative correlation of −0.233 at lag 21 days, while $\mathbf{p}_3^r$ is a slowly damping mode with auto-correlation decreasing monotonically and dropping to 0.3 at lag 10 days. As shown in Fig. 5b, mean seasonal cycles of standard deviation of the POP coefficients have the similarity between R1 and I2, further indicating that they should be treated together, and the EP mode will become more active during spring and early winter. The R3 index

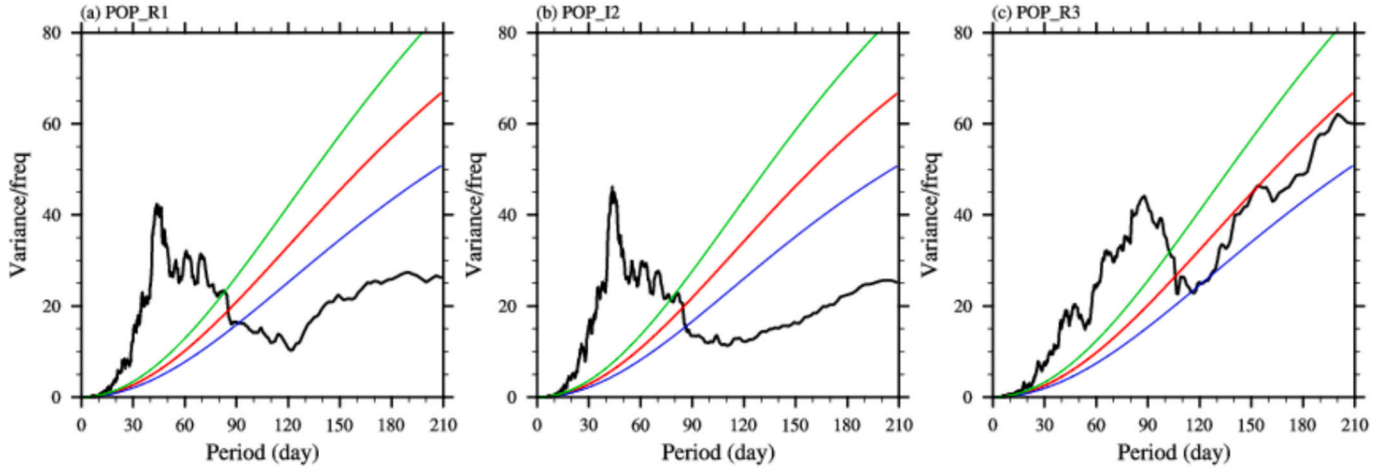

Fig. 6. Power spectra of time series of **a** R1, **b** I2, and **c** R3. The black line is the calculated spectrum, the red line is the "red noise" curve, the blue and green lines are the 5% and 95% "red noise" confidence bounds, respectively. (For interpretation of the references to color in this figure legend, the reader is referred to the web version of this article.)

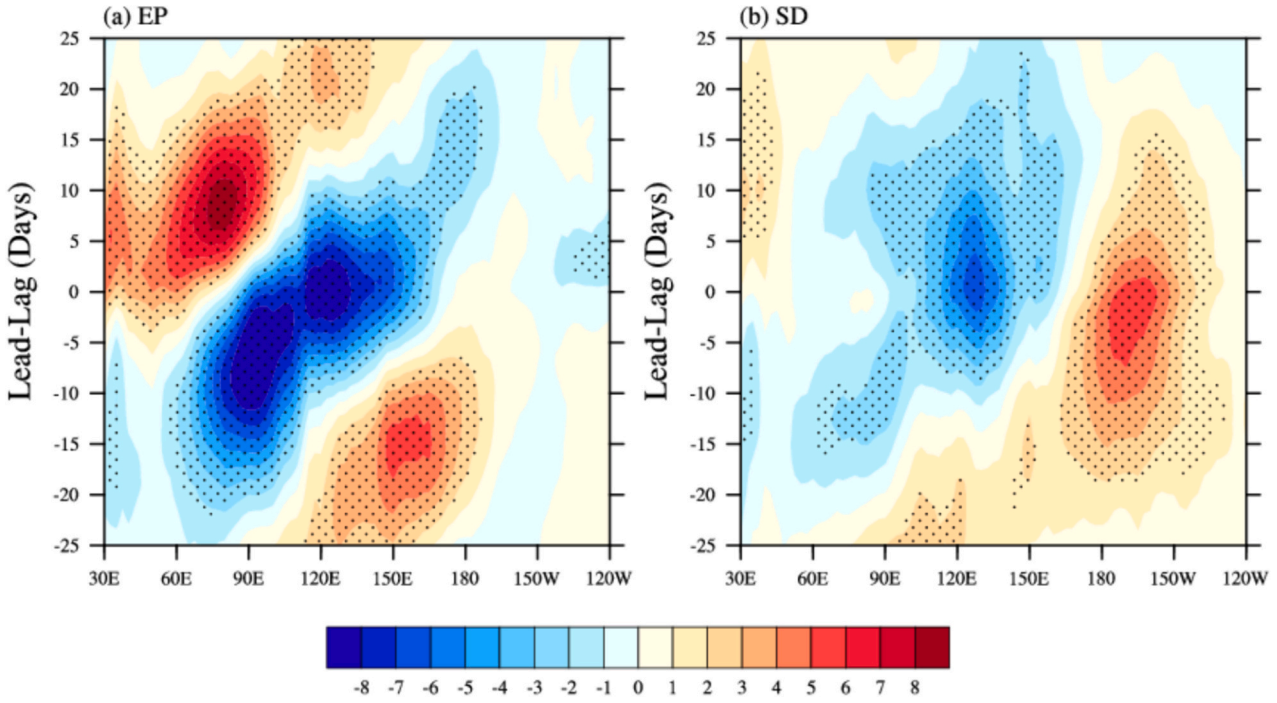

Fig. 7. Time-longitude regression diagrams of OLR (W m^{-2}) averaged over 15°S-15°N for **a** EP and **b** SD mode in boreal winter (NDFJMA). Results significant at the 95% confidence level are stippled.

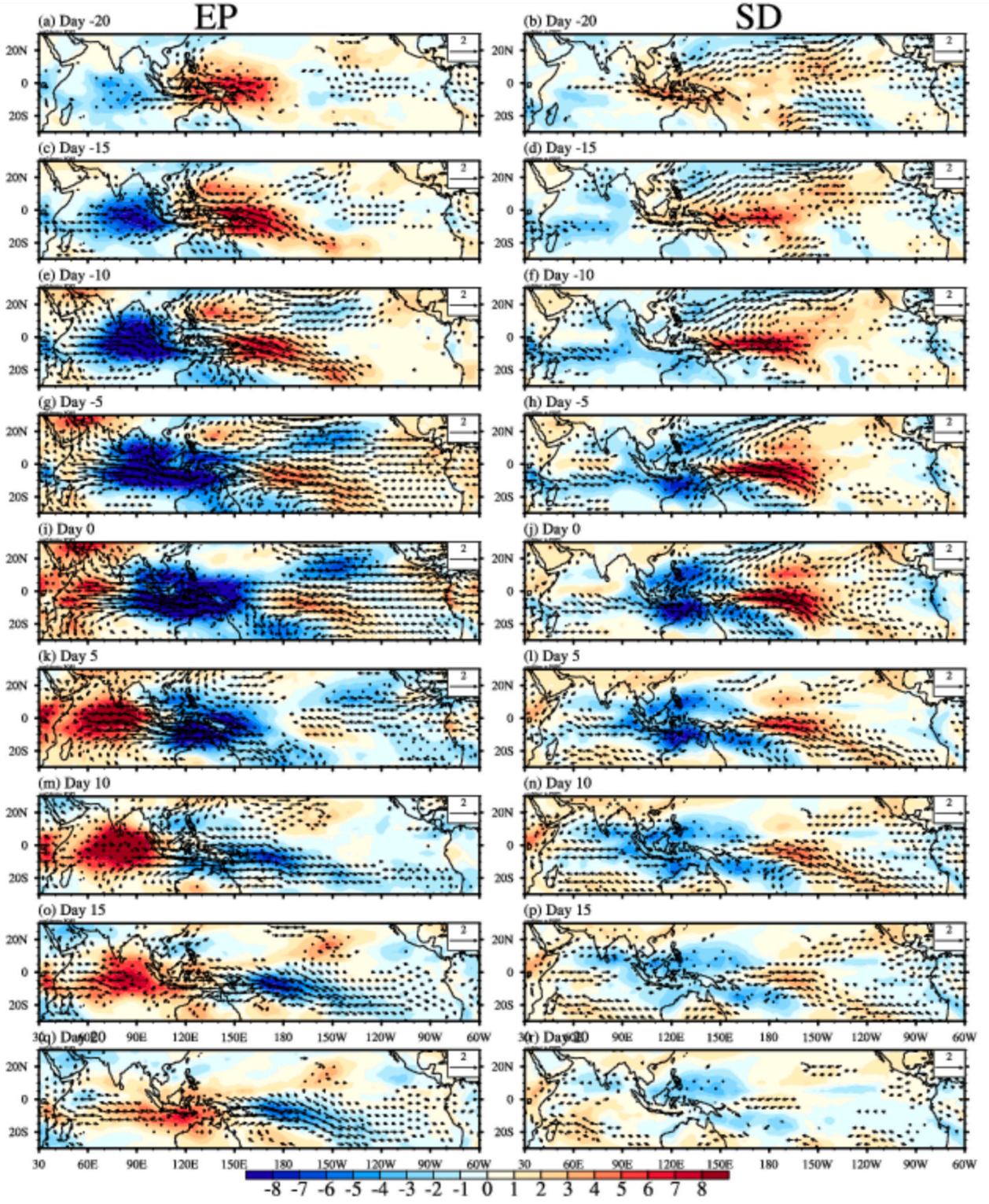

Fig. 8. Regression of OLR (color shading, W m^{-2}) and 850-hPa wind (vector, m s^{-1}) anomalies for (left) EP and (right) SD mode in boreal winter (NDFJMA). Stippling for OLR and vectors for wind mark results significant at the 95% confidence level.

has about half amplitude of R1 and I2, with a slightly different seasonality, which will be intensified during late winter and early summer.

Table 3 shows relationships between the POP time series and RMM indices. The correlations between R1/I2 with RMM1/RMM2 are higher than 0.9, confirming both the R1/I2 and RMM indices represent the eastward propagation of canonical MJO. Due to the property of POP, their eigenvectors are not orthogonal with each other. Therefore, the correlations between R3 and R1/I2 are not exactly equal to zero but reach quite low, which means that the SD mode is independent on the EP mode to a large degree. Power spectra of these POP time series are presented in Fig. 6. R1 and I2 are dominated by the intraseasonal timescale of 20–80 days peaking at ~45 days. Similarly, R3 has a significant period of 20–100 days but peaking at ~70 days, indicating a longer lasting feature as the SD mode.

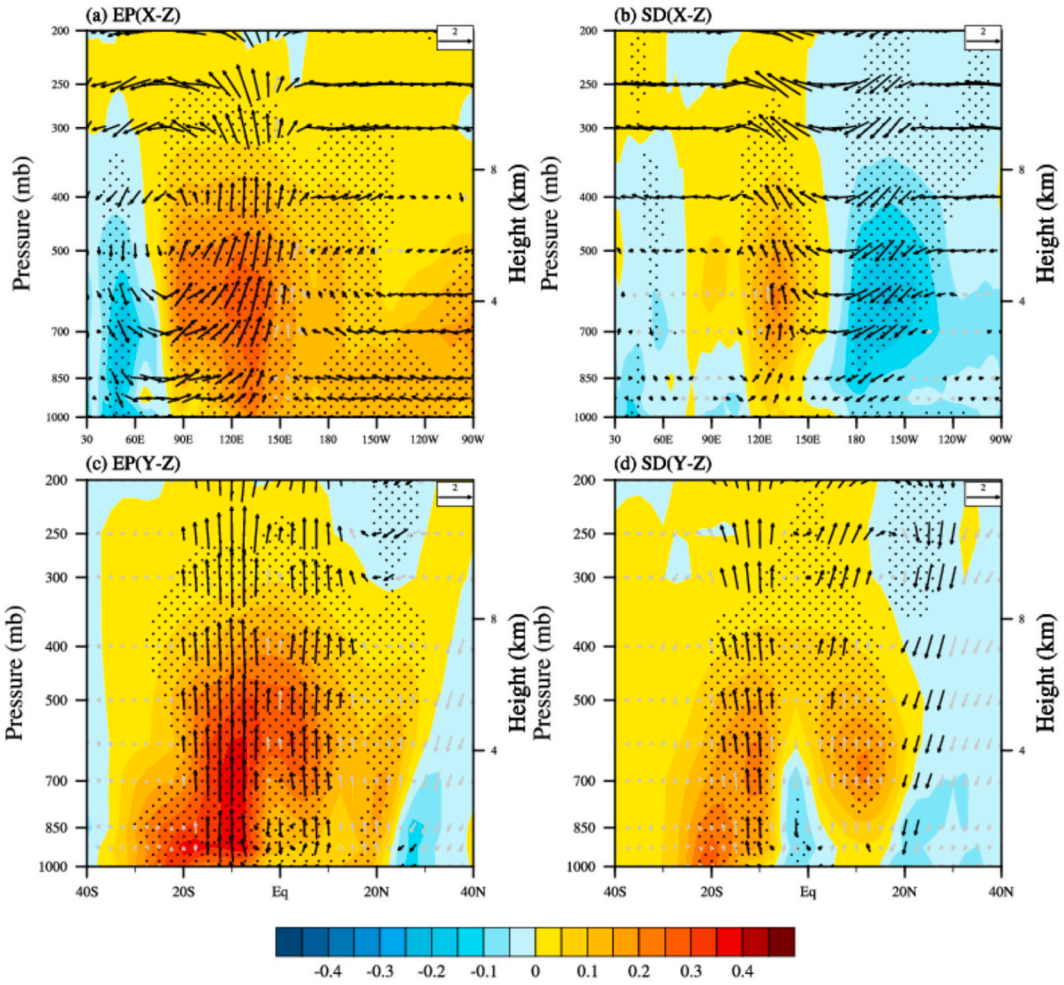

Fig. 9. Regression of **a, b** zonal-vertical distributions of anomalous (u,ω) averaged over 15°S-15°E and **c, d** meridional-vertical distributions of anomalous (v,ω) averaged over 110°E-130°E overlaid with specific humidity (color shaded, g kg^{-1}) in boreal winter (NDFJMA). Statistically significant results at the 95% confidence level are marked by black arrows for wind vectors and stippled for specific humidity. Vertical velocities are scaled by a factor of 200 to make them visible.

4. Spatial structures and time evolutions of the EP and SD modes

4.1. The regression patterns

Considering the significant seasonality of TISV (Wang and Xie, 1997; Lee et al., 2013; Adames et al., 2016) and the common active periods of the EP and SD modes (Fig. 5b), we will focus on the boreal wintertime (November–April, NDJFMA) in the rest of this paper. Fig. 7 shows the distinct zonal evolution characteristics of the two modes. For the EP mode, there is continuously eastward propagation of convection anomalies from the western IO to tropical CP, accompanied with the westward energy dispersion as featured by the amplitude of OLR anomaly envelope center (Adames and Kim, 2016). For the SD mode, the pattern of OLR anomalies is featured by a nearly stationary dipole with the enhanced convection located over MC and suppressed convection over tropical CP. An active SD event typically lasts for ~30 days, which is consistent with its decaying time scale detected by the POP analysis. Energy also seems to disperse westward for the SD mode, where featured by the envelop of OLR anomaly amplitude center consecutively evolves from the suppressed center over the tropical CP at day −5 to the enhanced center over MC at day 0 and then to the suppressed center over the western IO at day 10. Noted that A few of propagating signals can also be seen in Fig. 7b, which may attribute to the fact that the POP modes are not orthogonal to each other, and the timeseries of POPs are estimated by a least-square fit method, leaving some oscillation signal inevitably.

Lead-lag regressed spatial patterns of the OLR and low-level wind anomalies are shown in Fig. 8. For the EP mode, the large-scale negative OLR anomaly continually moves eastward from IO to WP along the equator, accompanied by a canonical low-level wind response pattern as equatorial Rossby and Kelvin waves. In contrast, for the SD mode, the negative OLR anomalies develop to the west of MC, sustain, and dissipate over MC without obvious propagation. The associated suppressed convection and low-level easterly anomalies over the tropical CP are stronger than those of the EP mode, maintaining their position and amplitude till the dissipation of convection over MC. In addition, compared to the EP mode, the negative OLR anomalies of the SD event over MC are located slightly off the equator but to its north and south sides.

The vertical structure patterns also show significant differences between the two modes once the anomalous convection centers approach MC, which can be clearly seen in the longitude-pressure (Figs. 9a-b) and latitude-pressure cross sections (Figs. 9c-d), respectively. For the EP mode, the backward tilting structure in moisture anomalies is clear together with the leading low-level positive anomalies in the east of convection. In contrast, such leading moisture structure diminishes for the SD mode, and instead, the negative anomalies of moisture and subsidence motion emerge in the tropical CP. These differences in the vertical structure of moisture and vertical motion to the east of convection center may be responsible for the distinct propagation features between the EP and SD modes, owing to the fundamental effects of anomalous moisture and upward motion in the planetary boundary

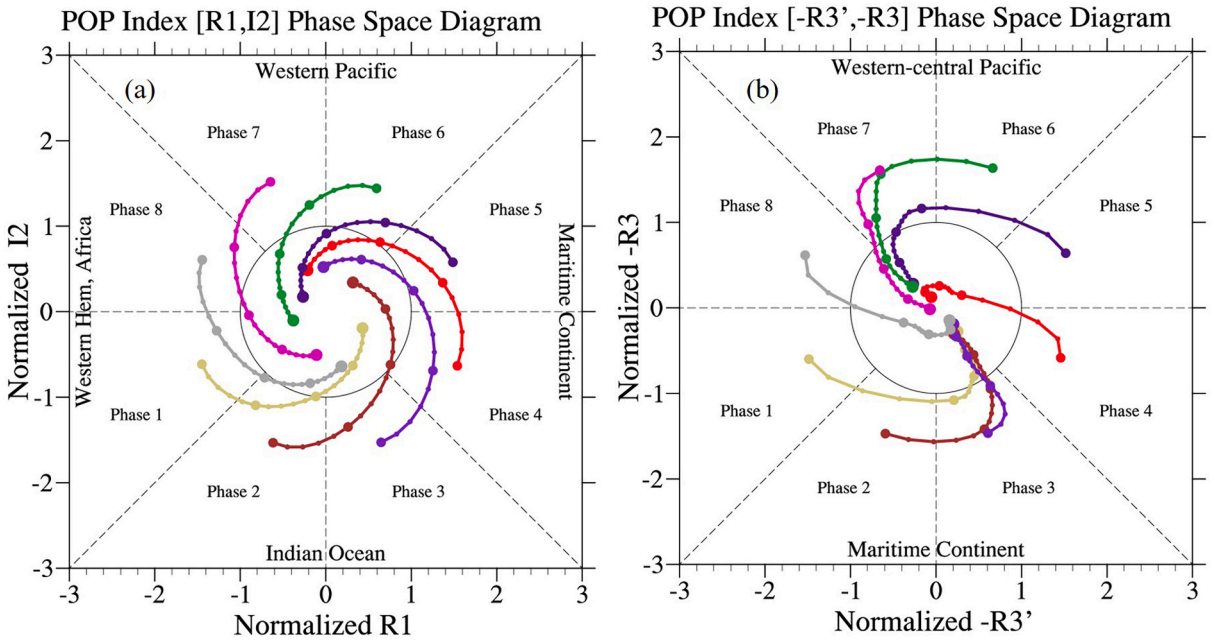

Fig. 10. **a** Normalized R1 and I2 phase composite curves of EP event. For each initial phases, strong cases are selected when the initial amplitude $(R1^2 + I2^2)^{½}$ exceeded $\sqrt{2}$. Then, data for each of the next 20 days from the initial day are averaged over all strong cases to show the evolution of the EP indices. **b** Same as **a** except for R3 and five-day running mean R3' phase composite curves of SD event.

layer (PBL) on the eastward propagation (Hsu and Li, 2012). In the latitude-pressure cross section, the mainly upward motion and positive moisture anomalies are concentrated on the equator and its south for the EP mode but are 10° off the equator at lower troposphere for the SD mode, which is consistent with the spatial convection structure shown in Fig. 8.

4.2. Composites in the phase space

To concisely illustrate time evolutions of the EP and SD modes, we construct the phase space composites similar with the methodology used for MJO by WH04. Here, a 5-day running mean is employed to remove high-frequency variability in the POP time series and all the analysis data. Composited evolutions of time series of the EP and SD modes are shown in Fig. 10. Given the high lead-lag correlations between R1 and I2 (Fig. 5), it is convenient to diagnose the state of EP mode as a point in the

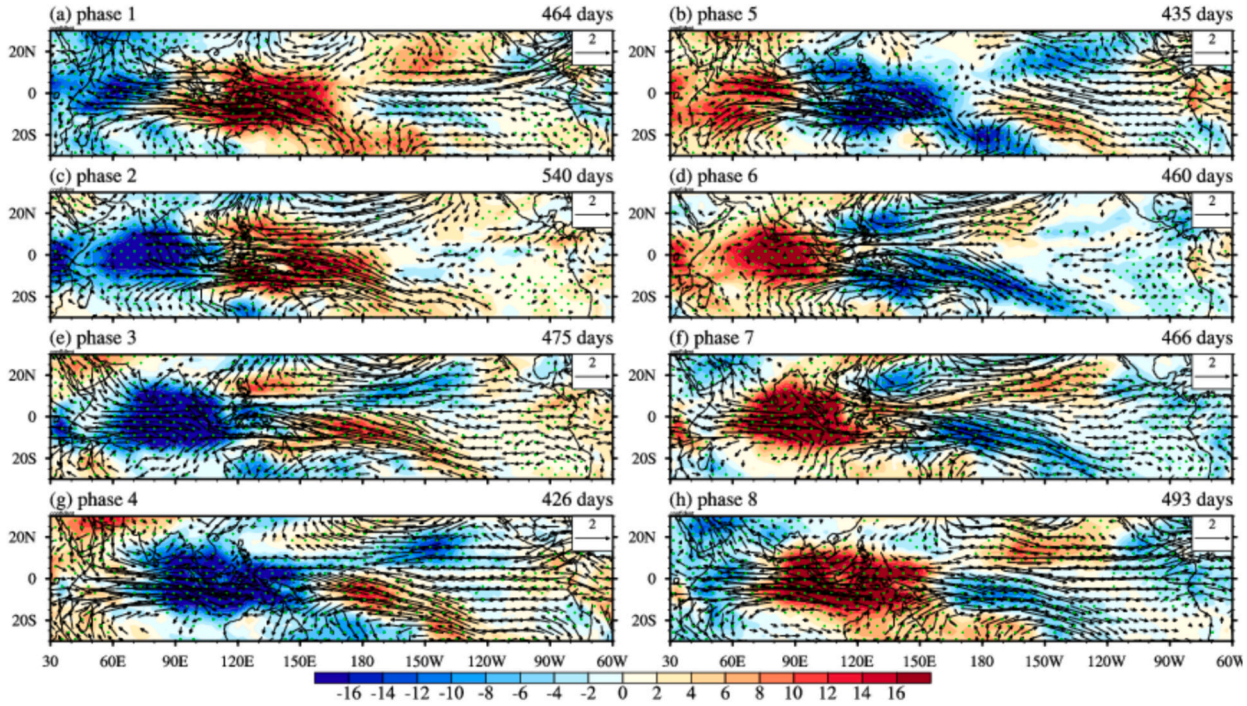

Fig. 11. Composite of anomalies in OLR (color shading, W m^{-2}) and 850-hPa wind (vector, m s^{-1}) for EP events in the phase space diagram of [R1, I2]. Stippling for OLR and vectors for wind mark statistically significant results at the 95% confidence level and the number of days falling within each phase category is given.

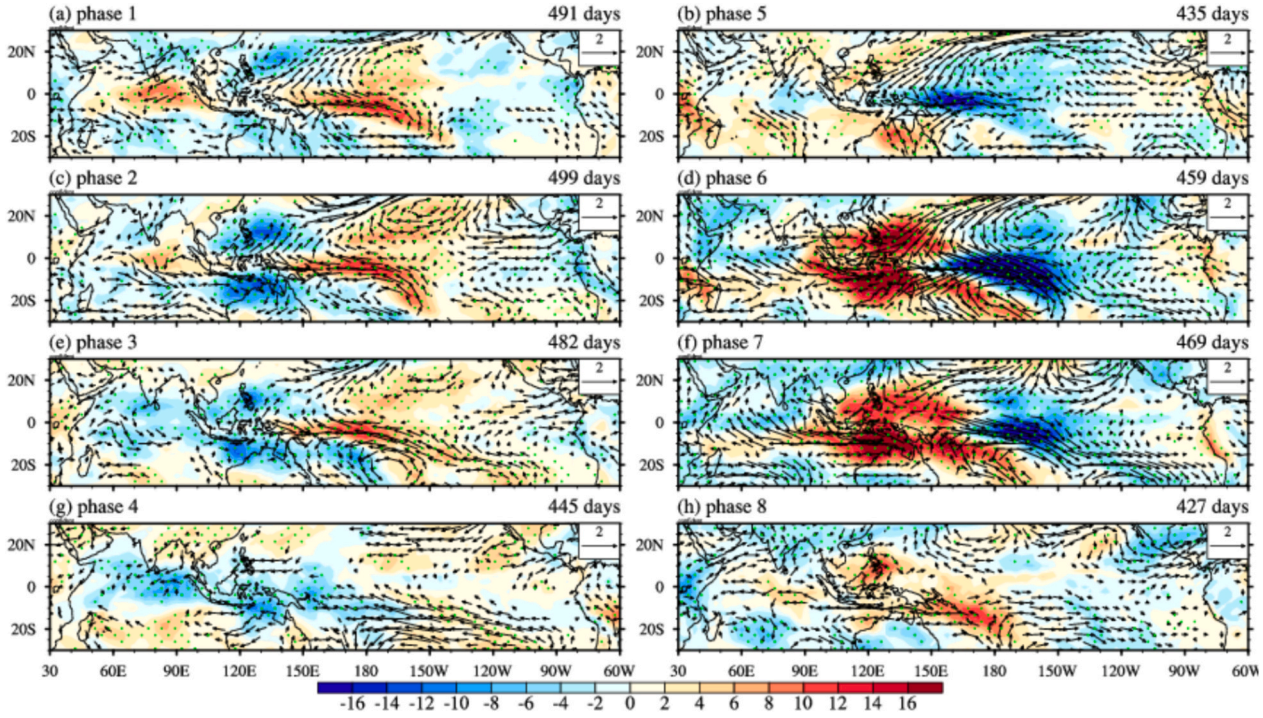

Fig. 12. Same as Fig. 11, but for the SD events in the phase space diagram of [−R3', −R3].

two-dimensional phase space defined by the normalized value pair of R1 and I2. Fig. 10a shows the composite curves in the phase space diagram of [R1, I2] for the strong EP states that have an initial amplitude greater than $\sqrt{2}$ (i.e., $(R1^2 + I2^2)^{½} > \sqrt{2}$). Following WH04, we can divide the phase space into eight phases and composite 20-day segments in each phase using the same approach as Wang et al. (2014). It is seen that the strong EP events can persist up to 15–20 days and propagate smoothly from one phase to next.

The phase space diagram for the EP mode could be established in a different way. Except for I2, an artificial time series that has a high lead-lag correlation with R1 can be created by R1 itself. Similarly, for the SD mode owning only one POP time series (R3), the two-dimensional phase space diagram of R3 can be established with its time tendency (denote as R3') using the centered finite difference method to show time evolution of those initial strong SD events (i.e., $(R3^2 + R3'^2)^{½} > \sqrt{2}$). It is convenient to infer the physical implication of each phase in Fig. 10b following the definition and combination position of R3 and R3'. To be specific, Phases 8–1 indicate the developing phase and Phases 2–3 represent the mature and decaying phases of positive SD events with the convection center located over MC. Phases 4–5 indicate the developing phase and Phases 6–7 represent the mature and decaying phases of negative SD events with the convection center over the tropical CP. It is evidently shown in Fig. 10b that the composited evolutions of SD events are quite distinct from the EP events. For instance, the SD event tends to decay more rapidly after passing through Phases 3 and 7 instead of propagating smoothly to the next phase as an EP event. These validate the definition of the SD mode of TISV as a stationary damping mode, instead of an oscillatory mode.

The composite patterns of OLR and 850-hPa circulation anomaly fields for each phase of the EP and SD modes are displayed in Fig. 11 and Fig. 12, respectively. The patterns of EP mode depict the canonical MJO structure and its evolution characteristics (Fig. 11). The enhanced convection builds over Africa and the western IO in Phase 1, moves eastward in the subsequent Phases 2–7 and decays over CP in Phase 8. The OLR patterns are generally symmetric with respect to the equator over IO and WP but shifts southward over western-central Pacific in Phases 7 and 8. However, for the SD mode (Fig. 12), the associated OLR anomalies are featured by the quasi-stationary enhanced and suppressed diploe pattern over MC and tropical CP, respectively. Here, we take Phases 1–4 (5–8) as the positive (negative) life cycle of SD events with the enhanced convection centered over MC (tropical CP). For the positive events, the significant low-level divergence and depressed convection first established on the equator over tropical CP, and then the enhanced convection developed to the south and north of equator around MC, accompanied by the anomalous cyclonic Rossby-wave pair. As magnitude of the anomalies decayed in Phase 3, the enhanced and depressed convection dipoles are still nearly standing in their locations. The negative SD events have a generally opposite evolution to the positive ones, except for the larger magnitude of convection anomalies, showing the existence of asymmetries in the SD events.

5. Application to real-time monitoring of TISV

Since none of traditional filtering method has been used, both EP (R1 and I2) and SD (R3) indices proposed in this study can be applied to real-time monitoring of TISV, which can be calculated as follows. Firstly, the real-time intraseasonal anomalies of OLR, U850 and U200 can be extracted by non-filtering method as described in section 2.2. Then, the three equatorial-averaged normalized intraseasonal anomaly fields are projected onto the observed 10 EOF patterns (Fig. 1) to obtain 10 PCs. Finally, based on the preserved POP vectors, the indices of EP and SD mode are calculated by a least-square fit as Eq. (10) and normalized by standard deviation of given years (e.g. 1981–2020). Selecting each of the typical EP and SD events, the corresponding indices and anomalous circulation patterns are analyzed in this section. Fig. 13 shows a lifecycle of the typical EP event in 2006. In the [R1, I2] phase space diagram, as seen in Fig. 13a, an EP event initiated from East Africa (Phase 1) in the first pentad of January 2006, then propagated to IO, amplified after passing through MC, reached WP and went into the western Hemisphere (Phase 8) in the second pentad of February. It takes ~40 days for this EP event to propagate around the equator, consistent with the period of typical MJO. The evolution of OLR and 850-hPa wind anomalies from January 5 to February 6 in 2006, as given in Fig. 13b, indicated that the convection propagated eastward along the equator and became stronger

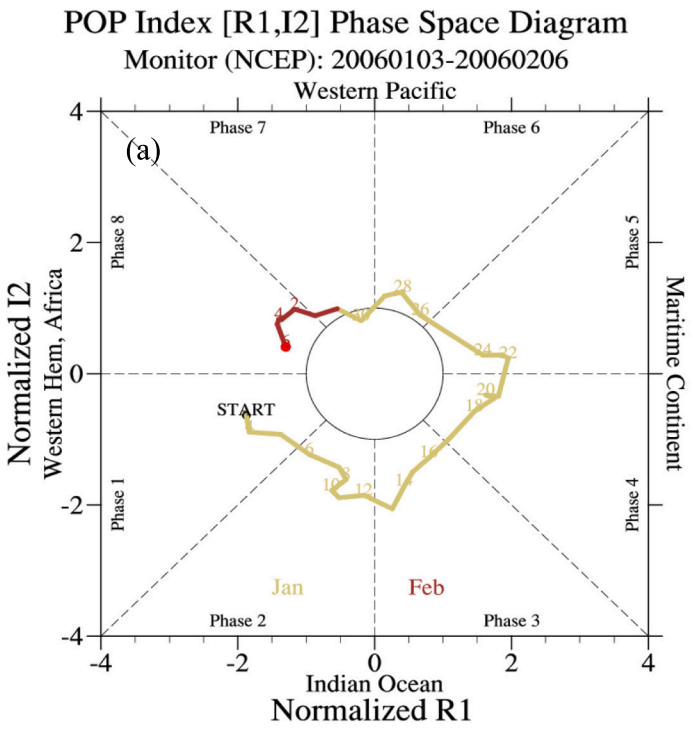

(b)

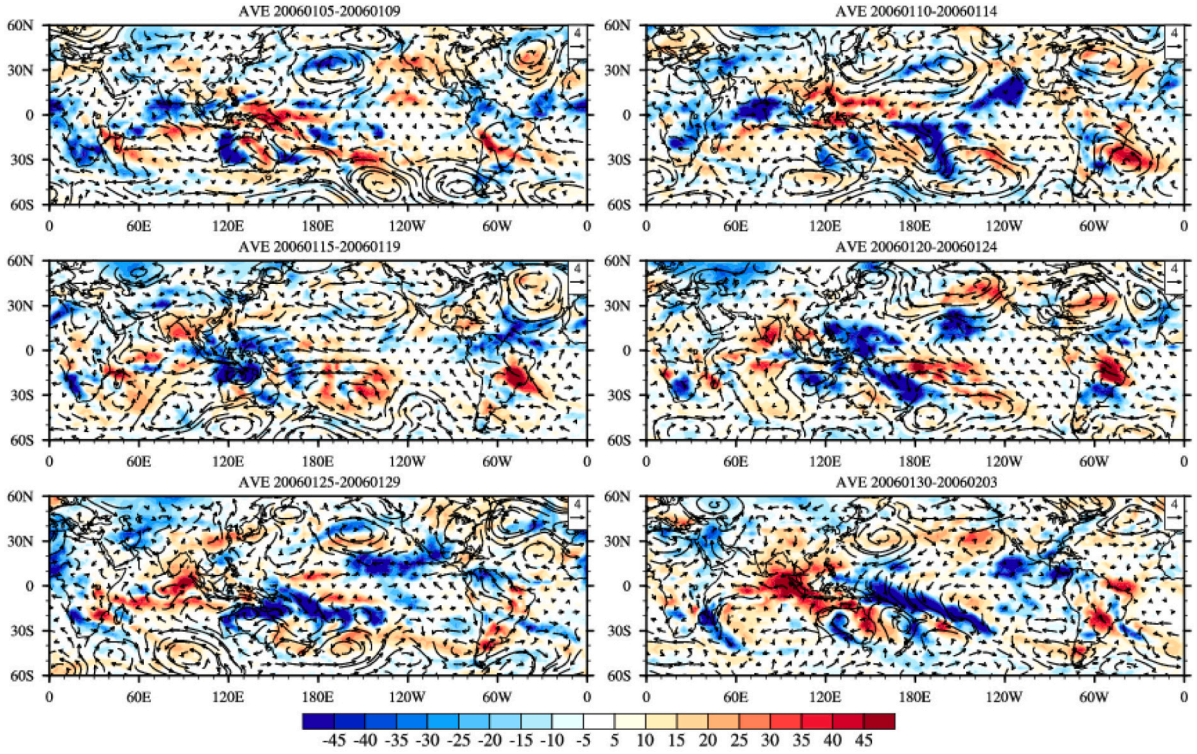

Fig. 13. Case study for an EP event. **a** [R1, I2] and **b** [R1, −R1'] phase space curves from January 3 to February 6, 2006, 5-day running mean was applied for R1'. **c** Pentad mean OLR (color shading, W m^{-2}) and 850-hPa wind (vector, m s^{-1}) anomalies from January 5 to February 3,2006.

when passing through MC, similar to the EP patterns composited in Fig. 11.

A typical positive SD event can be found in February 2008. The [−R3', −R3] phase space diagram (Fig. 14a) clearly represents the life cycle of this SD event: initiated around the second pentad of February from Phases 8 and 1, reached its peak on February 20, and gradually decayed in the last dekad of this month after passing through Phase 3. The corresponding convection and low-level circulation anomalies

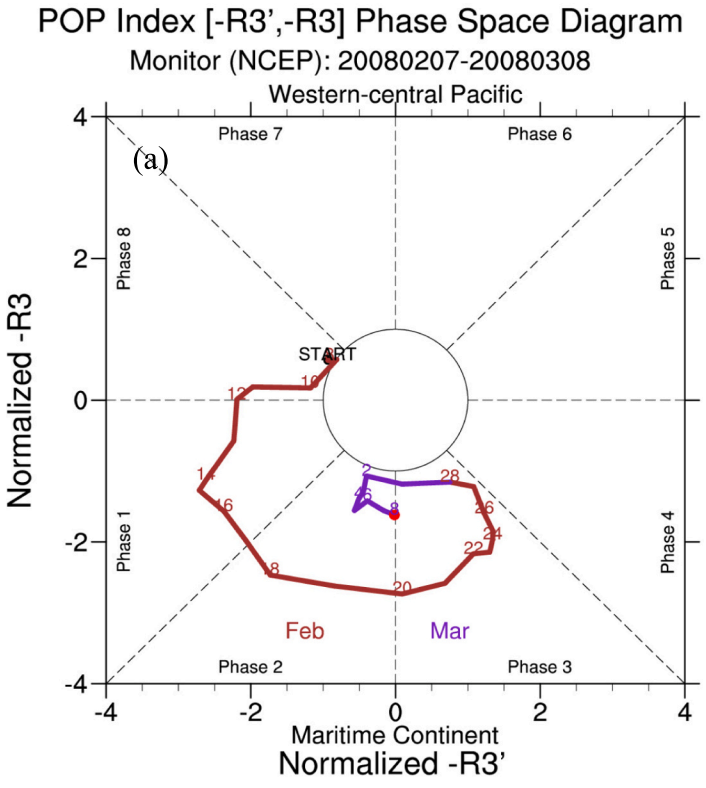

(b)

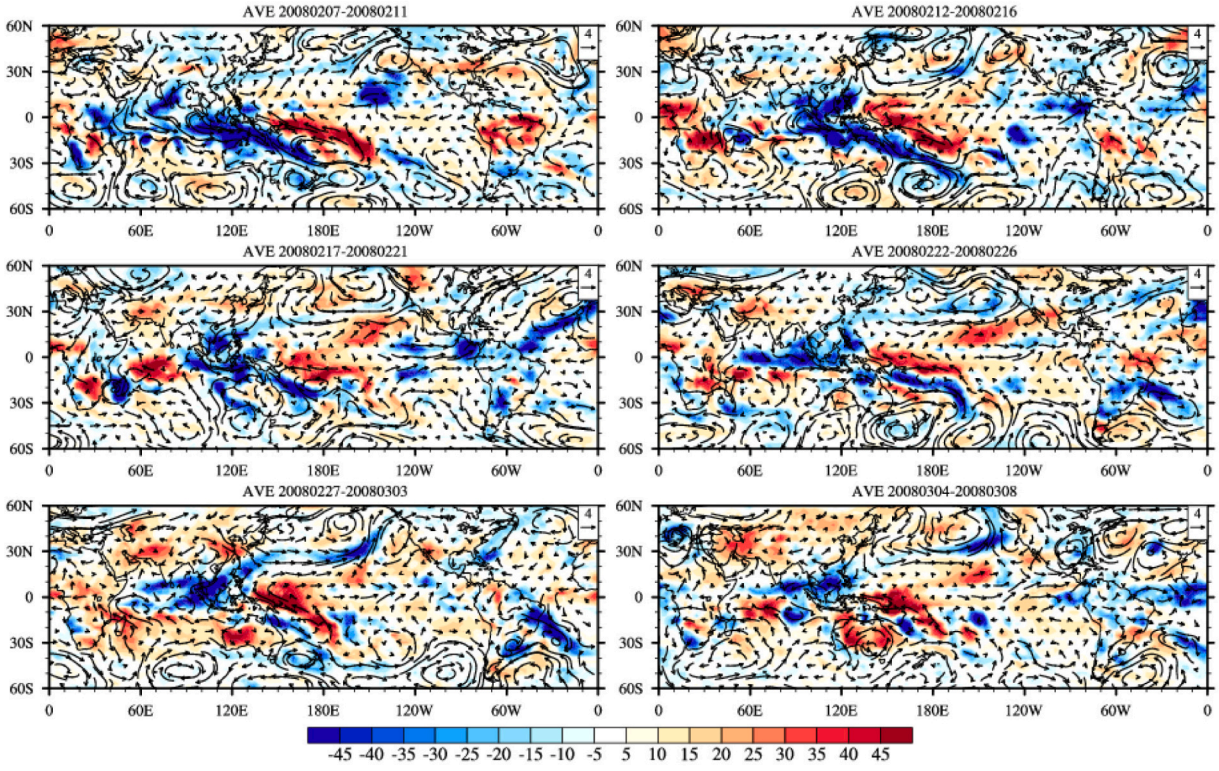

Fig. 14. Case study for a SD event. **a** [−R3', −R3] phase space curves from 7 February to 8 March, 2008. 5-day running mean was applied for R3'. **b** Pentad mean OLR (color shading, Wm^{-2}) and 850-hPa wind (vector, m s^{-1}) anomalies from 7 February to 8 March 2008.

clearly showed the SD structure with the enhanced convection centered over MC and depressed convection over the tropical CP (Fig. 14b). On the decaying stage, the active convection anomalies slightly shifted westward, while the suppressed convection and easterly wind anomalies hold their position and amplitude over the tropical CP throughout the event. In the meantime, less precipitation emerged over the southern and eastern China, as well as the eastern Australia due to the north-easterly and southeasterly wind anomalies responding to the convection anomalies over MC. Another case is the long-lasting snow-rainy event during January 2020, which bring more than twice precipitation over central and northern China (Zhao et al., 2020). During this period, a negative SD event is active with depressive convection over MC area, enhancing western Pacific subtropical high (WPSH) and transporting more moisture to the central and northern China (Fig.S3). Therefore, due to the standing characters of SD mode, it could be important for some long-last extreme event and may bring extra predictability. The teleconnections and influence of SD mode deserve further investigation in the future.

6. Summary and discussions

Given the great impacts on the global weather and climate events, TISV is one of the most important predictability sources for S2S prediction. Although MJO usually has been recognized as the dominant mode of TISV, it explains only about one-quarter fraction of total intraseasonal variance and shows large diversities especially when the convections arrive at MC region. Therefore, we have tried to reconsider this issue and investigated the leading modes with the long-lasting lifetime and large fraction variance in TISV. The two distinct leading modes with eastward propagating (EP) and standing dipole (SD) characteristics were identified based on the POP analysis in this study, and three real-time monitoring indices (two for the EP mode and one for the SD mode) were designed for the potential diagnosing and forecasting applications. These works may further shed light on the investigation of TISV and thus bring extra predictability source for the S2S prediction.

Apply POP analysis on the combined fields of equatorially averaged OLR, U850 and U200, two leading modes with long-lasting lifetime should be highlighted. The first one is an oscillatory mode with the period of 52 days and *e*-folding time of 19 days, which is denoted as the EP mode due to its consecutive eastward propagation characteristics. The second one is a non-oscillatory standing dipole mode with e-folding time of 13 days, which is denoted as SD mode. The EP and SD modes explain for about 46% and 12.3% variances of the EOF truncated variability. The real-time monitoring indices of EP and SD modes are proposed as the first 3 POP time series (R1 and I2 for the EP mode and R3 for the SD mode), which can be calculated by a least-square regression method. The R1 and I2 indices are tightly coupled with each other, while the R3 index is independent and nearly orthogonal to R1/I2 considering the weak correlations. The activity seasonal cycle is also slightly different for EP and SD modes, with large variance of EP mode presents in spring and early winter but in late winter and early summer for that of SD mode.

Because of the significant seasonality of TISV and the common active time range of EP and SD mode, the lead-lag regression and space phase composite analysis were applied in boreal wintertime (November to April) to investigate their different structures and evolution characteristics. The EP mode represents the canonical MJO features with smoothly eastward propagation of active convection from western IO to tropical Pacific along the equator. However, the SD mode mainly captures the standing convection dipole with the anomalies centered over MC and tropical CP. In particular, the convection anomalies of SD event over MC are located off the equator but to its north and south side during the peak stage. The vertical structures are also distinct for the EP and SD modes, as the leading moisture anomalies in PBL to the east of enhanced convection in the EP mode are diminished in the SD mode, and the upward movement and positive moisture anomalies are located off the equator over MC area for the SD mode.

Given the large lead-lag correlation between RI and I2, it is convenient to analyze the state of the EP mode in the two-dimensional phase space diagram of [R1, I2]. Similarly, the activity of SD mode can also be shown in the space phase diagram of R3 and its time tendency ([−R3', −R3']). The composite life cycles equally indicate the distinct characteristics of EP and SD modes. Specifically, the tracks of EP events can propagate smoothly from one phase to the subsequences, but the SD events will decay rapidly sooner after pass through Phases 3 and 7, confirming the SD events as non-oscillatory mode. Since no filtering method has been used, the EP (R1/I2) and SD (R3) indices proposed in this study can be apply to the real-time monitoring, and the case study well resembles the typical life cycle shown by regression and composite analysis.

Compared to previous studies using POP analysis (e.g. von Storch et al., 1988; von Storch and Xu, 1990), we highlight the long-lasting SD mode as the 3rd dominant POPs, which demonstrated distinct structure and propagation characteristic compared to the canonical EP mode and objectively identified the diverse nature of TISV. Recently, the research of the MJO diversity has also aroused increasing attentions (Kim et al., 2014; Zhang and Ling, 2017; Wang et al., 2019). In terms of propagation characteristics, the so called "non-propagation" or "standing" MJO may be the manifestation of the combination or the mixture of EP and SD mode, which need further investigation. The major conclusions in this study had been confirmed by repeated the calculation using ERA5 dataset (Hersbach et al., 2023). Further dynamic and moisture diagnosis and air-sea interaction analysis should be done to reveal the forming and maintaining mechanisms of SD mode. The extra-tropical teleconnection of EP and SD modes should also be different due to their distinct structure and evolution characteristics. Moreover, it is necessary to investigate the predictability and prediction skill of these modes in current operational dynamic modes. In addition, since POP analysis that considering the full spatio-temporal structure is more suitable to extract the instinct oscillation and decaying modes, it could also be further applied to analyze the mid- or high-latitude atmospheric variability and explore the possible undefined propagation and damping modes, which may be helpful for deepen our understanding on mid- and high-latitude dynamics. These issues will be explored in future studies.

CRediT authorship contribution statement

Jie Wu: Writing – original draft, Software, Methodology, Data curation, Formal analysis, Funding acquisition, Visualization. **Hong-Li Ren:** Writing – review & editing, Supervision, Conceptualization, Project administration, Funding acquisition. **Fei-Fei Jin:** Writing – review & editing, Conceptualization. **Xiaofeng Xu:** Supervision, Project administration. **Li Guo:** Writing – review & editing.

Declaration of competing interest

The authors declared that they have no conflicts of interest to this work. We declare that we do not have any commercial or associative interest that represents a conflict of interest in connection with the work submitted.

Data availability

The National Centers for Environmental Prediction/Department of Energy (NCEP/DOE) Reanalysis II dataset can be download from https://psl.noaa.gov/data/gridded/data.ncep.reanalysis2.html. The OLR data are daily-mean value from the National Oceanic and Atmospheric Administration (NOAA) polar-orbiting series of satellites can be download from https://psl.noaa.gov/data/gridded/data.olrcdr.interp.html.

Acknowledgements

This work was jointly supported by the China National Science Foundation Committee (42175052, U2242206), National Key Research and Development Program (2021YFA071800), China Meteorological Administration (CMA) Joint Research Project for Meteorological Capacity Improvement (23NLTSZ003), CMA Innovative Development Special Project (CXFZ2023J002), and CMA Youth Innovation Team (CMA2024QN06).

Appendix A. Supplementary data

Supplementary data to this article can be found online at https://doi.org/10.1016/j.atmosres.2024.107574.

References

Adames, A.F., Kim, D., 2016. The MJO as a Dispersive, Convectively coupled Moisture Wave: Theory and Observations. J. Atmos. Sci. 73, 913–941.
Adames, A.F., Wallace, J.M., Monteiro, J.M., 2016. Seasonality of the structure and propagation characteristics of the MJO. J. Atmos. Sci. 73, 3511–3526.
Feng, J., Li, T., Zhu, W.J., 2015. Propagating and non-propagating MJO events over Maritime Continent. J. Clim. 28, 8430–8449.
Fu, J.-X., Wang, W., Ren, H.-L., et al., 2018. Three different downstream fates of the boreal-summer MJOs on their passages over the Maritime Continent. Clim. Dyn. 51, 1841–1862.
Gehne, M., Kleeman, R., Trenberth, K.E., 2014. Irregularity and decadal variation in ENSO: a simplified model based on principal Oscillation patterns. Clim. Dyn. 43, 3327–3350.
Gottschalck, J., Wheeler, M., Weickmann, K., et al., 2010. A framework for assessing operational Madden–Julian oscillation forecasts: a CLIVAR MJO Working Group project. Bull Amer Meteor Soc. 91, 1247–1258.
Hersbach, H., Bell, B., Berrisford, P., Biavati, G., Horányi, A., Muñoz Sabater, J., Nicolas, J., Peubey, C., Radu, R., Rozum, I., Schepers, D., Simmons, A., Soci, C., Dee, D., Thépaut, J.-N., 2023. ERA5 hourly data on pressure levels from 1940 to present. Copernicus climate Change Service (C3S) climate data Store (CDS). https://doi.org/10.24381/cds.bd0915c6.
Hirata, F.E., Webster, P.J., Toma, V.E., 2013. Distinct manifestations of austral summer tropical intra-seasonal oscillations. Geophys. Res. Lett. 40, 3337–3341.
Hsu, H.H., Lee, M.Y., 2005. Topographic effects on the eastward propagation and initiation of the Madden-Julian Oscillation. J. Clim. 18, 795–809.
Hsu, P.C., Li, T., 2012. Role of the boundary layer moisture asymmetry in causing the eastward propagation of the Madden-Julian oscillation. J. Clim. 25 (14), 4914–4931.
Inness, P.M., Slingo, J.M., 2003. Simulation of the Madden–Julian Oscillation in a coupled General Circulation Model. Part I: Comparison with Observations and an Atmosphere-only GCM. J. Clim. 16, 345–364.
Jian, S., 1995. The Madden-Julian oscillation in the Canadian climate Centre general circulation model. Clim. Dyn. 12, 125–140.
Jiang, X., Adames, Á.F., Kim, D., Maloney, E.D., Lin, H., Kim, H., et al., 2020. Fifty years of research on theMadden-Julian Oscillation: Recentprogress, challenges, and perspectives.Journal of. Geophysical Research:Atmospheres 125 e2019JD030911.
Kanamitsu, M., Ebisuzaki, W., Woollen, J., et al., 2002. Ncep-Doe amip-Ii reanalysis (R-2). Bull. Amer. Meteor. Soc. 83, 1631–1643.
Kerns, B.W., Chen, S.S., 2016. Large-scale precipitation tracking and the MJO over the Maritime Continent and Indo-Pacific warm pool. J. Geophys. Res. Atmos. 121, 8755–8776.
Kim, D.H., Kug, J.S., Sobel, A.H., 2014. Propagating versus non-propagating Madden-Julian oscillation events. J. Clim. 27, 111–125.
Kim, H.-M., Kim, D., Vitart, E., et al., 2016. MJO propagation across the Maritime Continent in the ECMWF ensemble prediction system. J. Clim. 29, 3973–3988.
Kim, H.-M., Vitart, F., Waliser, D.E., 2018. Prediction of the Madden-Julian oscillation: a Review. J. Clim. 31, 9425–9443.
Lau, K.M., Waliser, D.E., 2012. Intraseasonal Variability of the Atmosphere–Ocean Climate System, 2nd edn. Springer, Heidelberg, Germany.
Lee, J.Y., Wang, B., Wheeler, M.C., et al., 2013. Real-time multivariate indices for the boreal summer intraseasonal oscillation over the Asian summer monsoon region. Clim. Dyn. 40, 493–509.
Liebmann, B., Smith, C.A., 1996. Description of a complete(interpolated) outgoing longwave radiation dataset. Bulletin ofthe American Meteorological Society 77, 1275–1277.
Lim, Y., Son, S., Kim, D., 2018. MJO prediction skill of the subseasonal-to-seasonal prediction models. J. Clim. 31, 4075–4094.
Lin, H., Brunet, G., Derome, J., 2008. Forecast Skill of the Madden–Julian Oscillation in two Canadian Atmospheric Models. Mon. Weather Rev. 136, 4130–4149.
Liu, P., 2014. MJO structure associated with the higher-order CEOF modes. Clim. Dyn. 43, 1939–1950.
Madden, R.A., Julian, P.R., 1971. Detection of a 40-50 day oscillation in the zonal wind in the tropical Pacific. J. Atmos. Sci. 28 (5), 702–708.
Madden, R.A., Julian, P.R., 1972. Description of global-scale circulation cells in the tropics with a 40-50 day period. J. Atmos. Sci. 29 (6), 1109–1123.
Newman, M., Sardeshmukh, P.D., Penland, C., 2009. How important is air–sea coupling in ENSO and MJO evolution? J. Clim. 22, 2958–2977.
Penland, C., Sardeshmukh, P.D., 1995. The optimal growth of tropical sea surface temperature anomalies. J. Clim. 8, 1999–2024.
Salby, M.L., Hendon, H.H., 1994. Intraseasonal behavior of clouds, temperature, and winds in the tropics. J. Atmos. Sci. 51, 2207–2224.
Seo, K.H., Wang, W., 2009. The Madden–Julian oscillation simulated in the NCEP climate Forecast System model: the importance of stratiform heating. J. Clim. 23, 4770–4793.
Sun, C., Li, J., Jin, F.-F., 2015. A delayed oscillator model for the quasi-periodic multidecadal variability of the NAO. Clim. Dyn. 45, 2083–2099.
von Storch, H., Xu, J.S., 1990. Principal oscillation pattern analysis of the tropical 30- to 60-day oscillation. Part I: Definition on an index and its prediction. Clim. Dyn. 4, 175–190.
Vitart, F., 2017. Madden–Julian Oscillation prediction and teleconnections in the S2S database. Q. J. R. Meteorol. Soc. 143, 2210–2220.
von Storch, H., Bruns, T., Fischer-Bruns, I., et al., 1988. Principal oscillation pattern analysis of the 30- to 60-day oscillation in General Circulation Model equatorial troposphere. J. Geophys. Res. Atmos. 93, 11022–11036.
von Storch, H., Burger, G., Schnur, R., et al., 1995. Principal oscillation patterns: A review. J. Clim. 8, 377–400.
Waliser, D., Sperber, K., Hendon, H., et al., 2009. MJO simulation diagnostics. J. Clim. 22, 3006–3030.
Wang, B., Xie, X.S., 1997. A model for the boreal summer intraseasonal ossciation. J. Atmos. Sci. 54, 72–86.
Wang, B., Chen, G., Liu, F., 2019. Diversity of the Madden-Julian oscillation. Sci. Adv. 5, eaax0220.
Wang, W.Q., Jang, P.H., Almazroui, M., 2014. Examination of multi-perturbation methods for ensemble prediction of the MJO during boreal summer. Clim. Dyn. 43, 2627–2637.
Wei, Y.T., Ren, H.-L., Xiang, B.Q., Wang, Y., Wu, J., Wang, S.G., 2023. Diverse MJO Genesis and Predictability. Bull Amer Meteor Soc. 104 (4), E792–E809. https://doi.org/10.1175/BAMS-D-22-0101.1.
Wheeler, M.C., Hendon, H.H., 2004. An all-season real-time multivariate MJO index: Development of an index for monitoring and prediction. Mon. Weather Rev. 132, 1917–1932.
Wu, J., Ren, H.-L., Zuo, J.Q., et al., 2016. MJO Prediction Skill, Predictability, and Teleconnection Impacts in the Beijing climate Center Atmospheric General Circulation Model. Dyn. Atmos. Oceans 75, 78–90.
Wu, J., Ren, H.-L., Jia, X., et al., 2023. Climatological diagnostics and subseasonal-to-seasonal predictions of Madden–Julian Oscillation events. Int. J. Climatol. 43 (5), 2449–2464.
Xu, J.-S., 1992. On the relationship between the stratospheric QBO and the tropospheric SO. J. Atmos. Sci. 49, 725–734.
Zhang, C.D., 2005. Madden-Julian Oscillation. Rev. Geophys. 43, RG2003.
Zhang, C.D., 2013. Madden-Julian Oscillation – bridging weather and climate. Bull. Amer. Meteor. Soc. 94, 1849–1870.
Zhang, C.D., Ling, J., 2017. Barrier effect of the Indo-Pacific Maritime Continent on the MJO: Perspectives from Tracking MJO Precipitation. J. Clim. 30, 3439–3459.
Zhao, J.H., Song, W.L., Ke, Z.J., 2020. Characteristics and causes analysis of the warm and wet winter in China in 2019/2020. J. Meteor Mon 46 (7), 982–993 (in Chinese).
Zhu, Z.W., Li, T., Hsu, P.-C., et al., 2015. A spatial–temporal projection model for extended-range forecast in the tropics. Clim. Dyn. 45, 1085–1098.